Solid-State Electronics 54 (2010) 1105–1112

Contents lists available at ScienceDirect

Solid-State Electronics

journal homepage: www.elsevier.com/locate/sse

High-temperature modeling of AlGaN/GaN HEMTs

S. Vitanov [a,*], V. Palankovski [a], S. Maroldt [b], R. Quay [b]

[a] *Advanced Material and Device Analysis Group, Inst. for Microelectronics, TU Wien, Gusshausstr. 27-29, 1040 Vienna, Austria*
[b] *Fraunhofer Inst. for Solid-State Physics (IAF), Tullastr. 72, 79108 Freiburg, Germany*

ARTICLE INFO

Article history:
Available online 11 June 2010

The review of this paper was arranged by Prof. A. Zaslavsky.

Keywords:
AlGaN/GaN
HEMT
High-temperature
Modeling
Simulation

ABSTRACT

Wide bandgap, high saturation velocity, and high thermal stability are some of the properties of GaN, which make it an excellent material for high-power, high-frequency, and high-temperature applications. As several application areas require the devices to operate at elevated temperatures, a proper modeling of the temperature dependences of the band structure and transport parameters is very important. We present two-dimensional hydrodynamic simulations of AlGaN/GaN high electron mobility transistors (HEMTs) at high temperatures. The simulator is calibrated against measurement data of a real device and delivers good predictive results for the DC and RF characteristics of another. The temperature dependence of the maximum current and cut-off frequency of submicron devices is further studied.

© 2010 Elsevier Ltd. All rights reserved.

1. Introduction

GaN takes advantage of the interesting material properties of the III-nitrides, such as a wide bandgap (3.4 eV), high breakdown electric field (4 MV/cm) and excellent thermal conductivity [1]. The latter two make GaN an interesting candidate for high-temperature systems. On the other hand, the high electron mobility (1600 cm^2/Vs) and high saturation velocity ($v_{sat} > 1.5 \times 10^7$ cm/s) give GaN an edge over other wide bandgap materials, as they allow RF operation of the devices. Consequently, outstanding results for the power density in GaN HEMTs have been reported in the last few years, e.g. 8.6 W/mm at the Ka-band [2] and 40 W/mm at the C-band [3], and the devices are considered for high-power high-frequency applications at elevated temperatures [4].

Several groups have studied the high-temperature DC operation of AlGaN/GaN HEMTs on different substrates (sapphire [5–7], SiC [6] and Si [7,8]).

AC measurements at elevated temperatures however are sparse: e.g. the temperature dependence of the cut-off frequency is compared to that of the transconductance by Akita et al. [9]. An investigation of the influence of high temperature on the microwave power performance of AlGaN/GaN HEMTs is conducted by Arulkumaran et al. [10].

On the other hand, the theoretical studies of GaN-based transistors at higher temperature are also rare. There are few analytical models developed [11–13], however those are tailored for use in circuit simulation, not for device optimization. To our knowledge there is only one work, which focuses solely on high-temperature HEMT device simulation [14], however it relies on dated experimental data [9] and does not feature AC performance.

In the subsequent study the material and model parameters for GaN and AlGaN are discussed. They are incorporated in the two-dimensional device simulator Minimos-NT [15]. The simulator is then calibrated against measurement data of a state-of-the-art $l_g = 0.25$ μm device at room and elevated temperatures. Using the same set of models and parameters predictive simulations for a $l_g = 0.5$ μm device are conducted. Good agreement for the DC and AC characteristics is achieved. Further, the temperature dependence of the drain current and cut-off frequency on the gate length is theoretically studied for sub-quartermicron devices.

2. Physical and material models

We perform two-dimensional hydrodynamic electro-thermal simulations with our device simulator Minimos-NT, which proved to be a suitable tool for the analysis of heterostructure devices [16]. We have used it for the optimization of field-plate structures [17] and the design of new device generations [18].

Our choice of transport model aims to achieve maximum accuracy combined with computational efficiency. Since the drift-diffusion transport model is not able to deliver accurate results for submicron GaN FETs [19,20], we employ the hydrodynamic transport model. As AlGaN/GaN HEMTs are unipolar devices, computational effort is reduced by neglecting the equations for holes in this work. Self-heating effects are accounted for by the lattice heat flow equation. It is obtained from the stationary energy flux balance derived

* Corresponding author. Tel.: +43 15880136017; fax: +43 15880136099.
E-mail addresses: vitanov@iue.tuwien.ac.at (S. Vitanov), palankovski@iue.tuwien.ac.at (V. Palankovski).

0038-1101/$ - see front matter © 2010 Elsevier Ltd. All rights reserved.
doi:10.1016/j.sse.2010.05.026

from the second moment solving the Boltzmann transport equation and the carrier continuity equation. The heat generation is expressed as the sum of the energy relaxation approximation of the scattering terms of the Boltzmann equation and the effective recombination. The hydrodynamic transport model is derived from the Boltzmann equation by taking into account the first four moments of the distribution function. In order to obtain a closed equation set the heated Maxwellian distribution is assumed [21]. A macroscopic relaxation time approximation is used.

Finally, a system of four partial differential equations: Poisson, current continuity and energy balance for electrons, and the lattice heat flow equation, is solved self-consistently. For the heat flow, Neumann boundary conditions are assumed at all device boundaries. The only exception is the bottom boundary, where an additional thermal contact is introduced, which models the heat flow into the substrate. The lattice temperature is calculated using a specified contact temperature (equal to the ambient temperature in our simulations) and a thermal resistance. The latter represents the lumped thermal resistance of the nucleation layers and the substrate. The thermal heat-flow across the boundary is accounted for self-consistently.

The four differential equations have material-specific parameters, such as bandgap energy, electron mobility, thermal conductivity, etc. The dependence of these parameters on temperature, energy, etc. is described by models, which are presented in the following.

2.1. Bandgap energy

The Varshni formula describes well the temperature dependence of the band gap in nitrides. The temperature dependence of the bandgap is calculated by:

$$E_\mathrm{g} = E_{\mathrm{g},0} - \frac{\alpha_\mathrm{g} T_\mathrm{L}^2}{\beta_\mathrm{g} + T_\mathrm{L}}.$$

The values for $E_{\mathrm{g},0}$ (energy band gap at 0 K), α_g and β_g (empirical constants) for GaN and AlN are shown in Table 1. The parameter values for GaN are an average of various reported results as summarized in [22], while those for AlN are based on the experimental work of Guo et al. [23]. The bandgap of $\mathrm{Al}_x\mathrm{Ga}_{1-x}\mathrm{N}$ is then interpolated by:

$$E_\mathrm{g}^\mathrm{AlGaN} = E_\mathrm{g}^\mathrm{AlN}(1-x) + E_\mathrm{g}^\mathrm{GaN}x + C_\mathrm{g}(1-x)x,$$

with the bowing parameter C_g. The reported values of the latter show a large variation ranging from −0.8 [24] to 1.33 [25]. However, several experiments [26,27] show a linear variation ($C_\mathrm{g} \approx 0$), which is adopted here.

An energy offset (E_off) is used to align the valence band of different materials. For $\mathrm{Al}_x\mathrm{Ga}_{1-x}\mathrm{N}$ it is calculated by:

$$E_\mathrm{off}^\mathrm{AlGaN} = \frac{E_\mathrm{off}^\mathrm{AlN}\left(E_\mathrm{g}^\mathrm{AlGaN} - E_\mathrm{g}^\mathrm{GaN}\right) - E_\mathrm{off}^\mathrm{GaN}\left(E_\mathrm{g}^\mathrm{AlGaN} - E_\mathrm{g}^\mathrm{AlN}\right)}{E_\mathrm{g}^\mathrm{AlN} - E_\mathrm{g}^\mathrm{GaN}},$$

where $E_\mathrm{off}^\mathrm{GaN}$ and $E_\mathrm{off}^\mathrm{AlN}$ are the offset energies for GaN and AlN, respectively. As the valence band edge of GaN is chosen as reference, $E_\mathrm{off}^\mathrm{GaN}$ is set to 0 eV. The valence-band-offset of AlN $E_\mathrm{off}^\mathrm{AlN}$ is chosen as 1.12 eV, which is equal to 40% of the total bandgap discontinuity as reported by Westmeyer et al. [28]. For $\mathrm{Al}_x\mathrm{Ga}_{1-x}\mathrm{N}$ with $x = 0.22$, the valence-band-offset against GaN is 0.25 eV (further, our setup provides a value of 0.225 eV for $x = 0.2$, which is in a good agreement with the experimentally determined offset of 0.25 eV [29] for the same composition). We have experimentally determined the barrier height of the Schottky contact to GaN to be 1.0 eV at room temperature in agreement with experiments by other groups [30]. The changes in the barrier height with temperature (in the range under investigation) are negligibly small [31].

2.2. Spontaneous and piezoelectric polarization

A good understanding of the electrical polarization effects at the $\mathrm{Al}_x\mathrm{Ga}_{1-x}\mathrm{N}$/GaN interface is a key to the proper device simulation. The spontaneous polarization P_SP and the strain-induced piezoelectric polarization P_PZ are calculated by:

$$P_\mathrm{SP} = P_\mathrm{SP,AlN} + P_\mathrm{SP,GaN}(1-x),$$
$$P_\mathrm{PZ} = 2 \cdot \frac{a - a_0}{a_0}\left(e_{31} - e_{33} \cdot \frac{C_{13}}{C_{33}}\right),$$

where a and a_0 are the lattice constants, e_{13} and e_{33} are the piezoelectric coefficients, C_{13} and C_{33} denote the elastic constants. The methodology and the parameter values are after [32,33]. The total polarization-induced sheet charge density at the $\mathrm{Al}_{0.22}\mathrm{Ga}_{0.78}\mathrm{N}$/GaN interface calculated by using these expressions is $1.23 \times 10^{13}\ \mathrm{cm}^{-2}$. In the real device however, several effects (such as dislocations or surface states) can significantly reduce this value. Therefore, after calibration against the measurement data, we adopt a sheet charge density of $9.5 \times 10^{12}\ \mathrm{cm}^{-2}$ at the channel/barrier interface and a complementary charge density of $-2.5 \times 10^{12}\ \mathrm{cm}^{-2}$ at the barrier/cap interface.

The dependence of the spontaneous polarization coefficients for GaN and AlN on temperature has been measured to be minimal [33,34]. There are also no reports on the piezoelectric polarization at higher temperatures. Hence, we retain the same sheet charge density values for higher temperatures too.

2.3. Thermal conductivity

The thermal conductivity is modeled by a power law:

$$\kappa(T_\mathrm{L}) = \kappa_{300} \cdot \left(\frac{T_\mathrm{L}}{300\ \mathrm{K}}\right)^{\alpha},$$

where κ_{300} is the value at 300 K. From early experiments, a $\kappa_{300} = 130$ W/mK for 'bulk' GaN [35] was extracted. However, later measurements of epitaxial structures yielded higher values [36], and a strong dependence on the dislocation density was observed [37]. Based on various studies [35,36,38–41] we give two parameter sets in Table 2, applicable for different material quality. Fig. 1 compares the two model sets with other models and experimental data (model 1 is used in the simulations). For AlN the variation of the measured values for the thermal conductivity is smaller (Fig. 2). We assume a κ_{300} of 350 W/mK, which is close to the value reported by [42]. The parameter α, which models the decrease with temperature is calibrated against measured data [42–44].

Table 1
Summary of band structure parameters.

Material	$E_{\mathrm{g},0}$ (eV)	α_g (eV/K)	β_g (K)
GaN	3.4	9.09×10^{-4}	800
AlN	6.2	18.0×10^{-4}	1462

Table 2
Summary of thermal properties.

Material	κ_{300} (W/m K)	α
GaN model 1	130	−0.43
GaN model 2	220	−1.2
AlN	350	−1.7

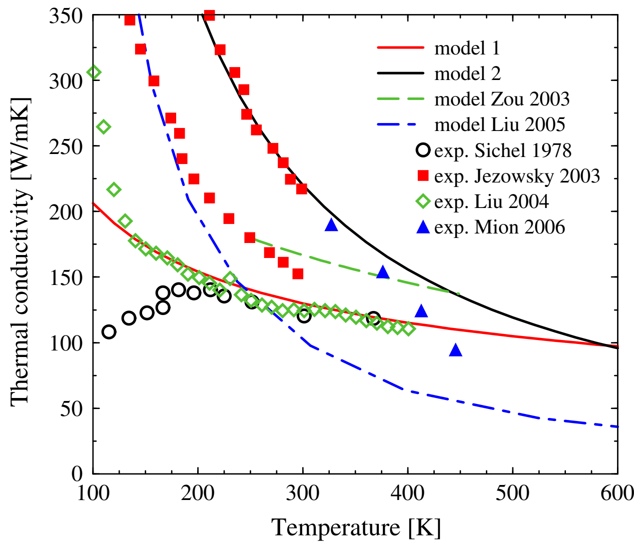

Fig. 1. GaN thermal conductivity as a function of temperature.

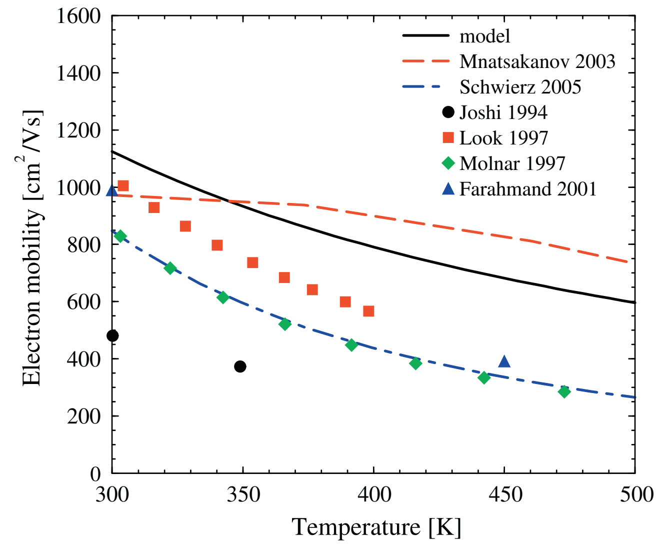

Fig. 3. Low-field bulk mobility in GaN as a function of lattice temperature.

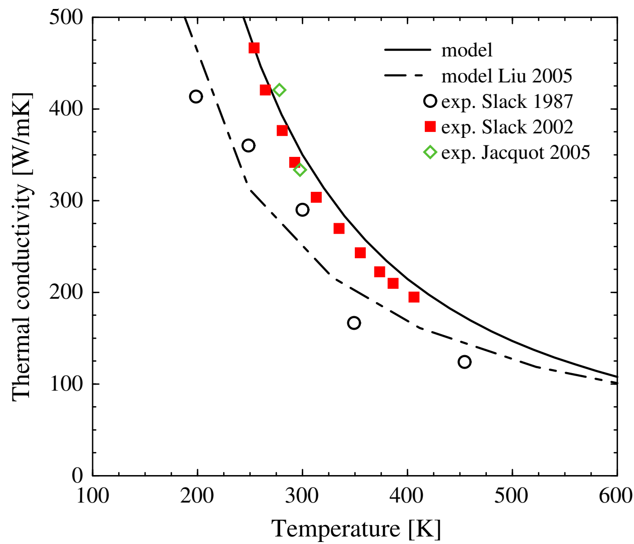

Fig. 2. AlN thermal conductivity as a function of temperature.

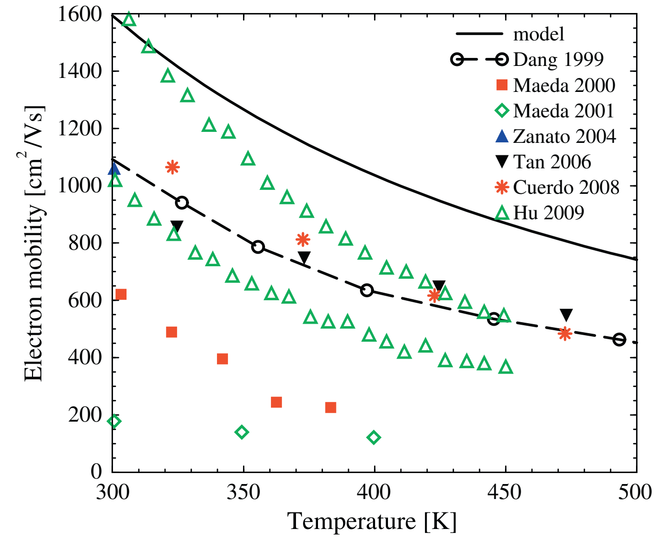

Fig. 4. Low-field 2DEG mobility at the AlGaN/GaN interface as a function of lattice temperature.

2.4. Mobility model

The low-field mobility is modeled by an expression similar to that proposed by Caughey and Thomas [45,16]:

$$\mu^{\mathrm{LI}} = \mu^{\mathrm{min}} + \frac{\mu^{\mathrm{L}} - \mu^{\mathrm{min}}}{1 + \left(C_{\mathrm{I}}/C^{\mathrm{ref}}\right)^{\gamma_0}}.$$

C_{I} denotes the concentration of ionized impurities, μ^{L} is the mobility in undoped material, μ^{min} is the mobility in highly doped material, limited by impurity scattering. In order to model the temperature dependence the mobilities are additionally parameterized using power laws:

$$\mu^{\mathrm{L}} = \mu^{\mathrm{L}}_{300}\left(\frac{T_{\mathrm{L}}}{300\ \mathrm{K}}\right)^{\gamma_1}, \quad \mu^{\mathrm{min}} = \mu^{\mathrm{min}}_{300}\left(\frac{T_{\mathrm{L}}}{300\ \mathrm{K}}\right)^{\gamma_2}.$$

Similar expressions have been used also by others [46,47]. To calibrate the γ_1 and γ_2 parameters we rely on our own Monte Carlo simulation, which consider a high-quality material [48]. Monte Carlo (MC) simulations by other groups [46,49] and experiments [50,51] for the electron mobility in bulk GaN as a function of the temperature are shown in Fig. 3. Over the years the electron mobilities increase due to the improved quality of the material samples. Models proposed by other groups [47,52] are also displayed. Fig. 4 shows the electron mobility as a function of temperature in the two-dimensional electron gas (2DEG) as experimentally determined by various groups [53–57,8]. The 2DEG mobility exhibits overall higher values especially at high temperatures, while retain-

Table 3
Summary of low-field mobility model parameters for GaN.

μ^{L}_{300}	μ^{min}_{300}	γ_0	γ_1	γ_2
1600 cm²/Vs	100 cm²/Vs	0.065	−1.5	−0.2

ing the trend for improved results over time. The parameter values we choose are listed in Table 3. The maximum (μ^{L}_{300}) and minimum mobility (μ^{min}_{300}) are calibrated against our own MC simulation. A decrease of the maximum mobility with temperature ($\gamma_1 = -1.5$), in agreement with the power term of the acoustic phonon mobility expression [58] is assumed. Our MC simulation results and recent experiments from [59] confirmed that the latter is the dominant scattering mechanism at high temperatures. A weak temperature dependence ($\gamma_2 = -0.2$) of the electron mobility at high concentrations is adopted.

A two-valley hydrodynamic mobility model describes the high-field electron transport. It is derived from the high-field mobility model using the local energy balance equation:

$$\mu_v(T_n) = \frac{2 \cdot \mu_v^{LI}}{2 + a_v + \sqrt{a_v \cdot (4 + a_v)}}, \quad v = \Gamma, U,$$

$$a_v = \frac{3 \cdot k_B \cdot \mu_v^{LI} \cdot (T_n - T_L)}{2 \cdot q \cdot \tau_v \cdot (v_{sat,v})^2},$$

where μ_v^{LI}, τ_v, and $v_{sat,v}$ are the valley-specific low-field mobilities, relaxation times, and saturation velocities. A weighted mean is then built:

$$\mu = \frac{\mu_\Gamma + \mu_U \cdot P_U}{1 + P_U}.$$

The coefficient P_U defines the dominant mobility (μ_Γ is the mobility in the lowest Γ valley, μ_U is the mobility in the next ML valley) dependent on the valley occupancy:

$$P_U = 6 \cdot \left(\frac{m_U^*}{m_\Gamma^*}\right)^{3/2} \cdot \exp\left(-\frac{\Delta E_C}{k_B \cdot T_n}\right).$$

m_U^* and m_Γ^* are the electron masses in the respective valleys, T_n the electron energy.

The model delivers an acceptable approximation in comparison to MC simulations, accounting for six bands [58] (Fig. 5). Results from different groups vary largely (e.g. peak velocity from 2.5×10^7 cm/s to 3.5×10^7 cm/s), therefore our goal is not a perfect agreement with this particular MC simulation. The model is a carefully chosen trade-off. It provides a velocity-field characteristics close to the one obtained by MC simulation on the one hand,

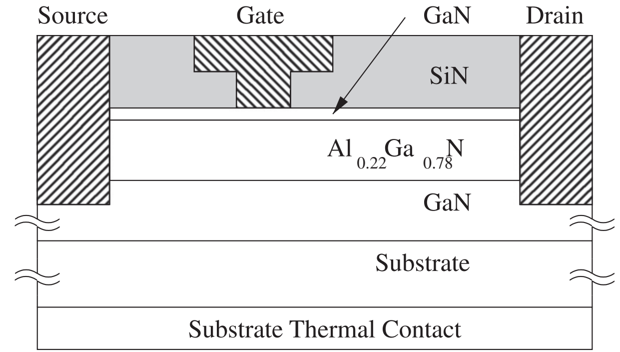

Fig. 6. Schematic layer structure of the investigated device.

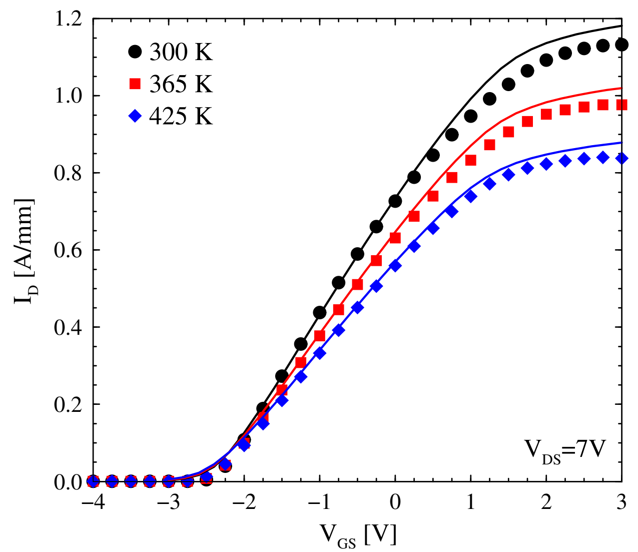

Fig. 7. Calibrated transfer characteristics versus experimental data (symbols) for l_g = 0.25 μm HEMT.

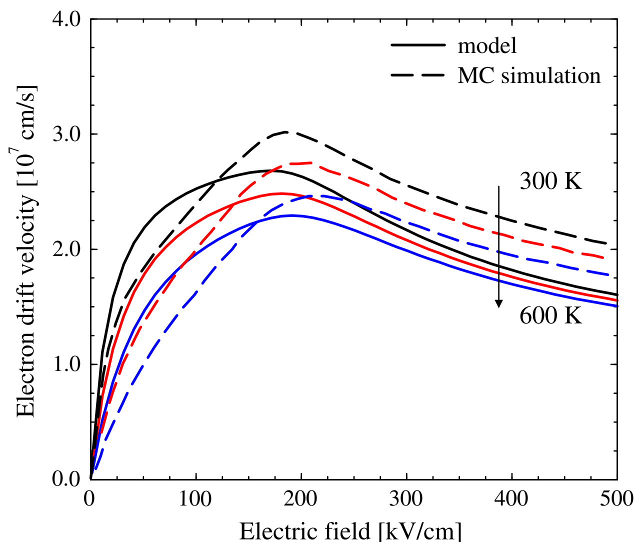

Fig. 5. Electron drift velocity versus electric field for lattice temperature of 300, 450 and 600 K.

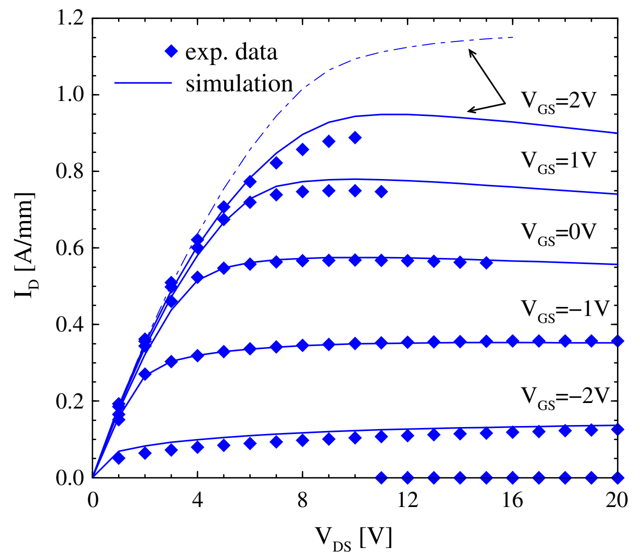

Fig. 8. Calibrated output characteristics versus experimental data for l_g = 0.25 μm HEMT at 425 K. Dot-dashed line-w/o self-heating, solid line-with self-heating.

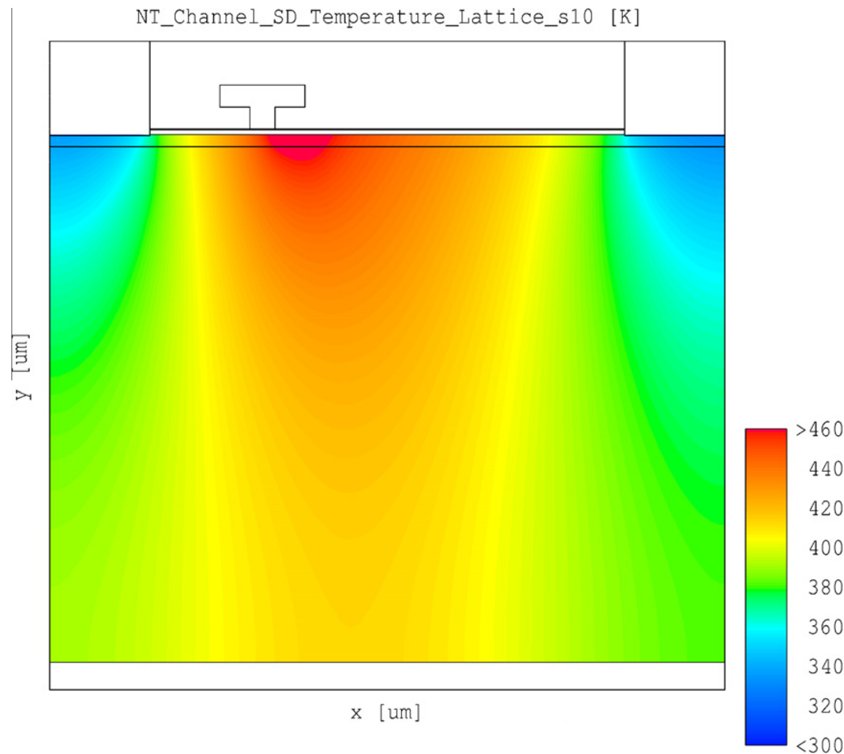

Fig. 9. Lattice temperature, calibration device, $V_{GS} = 2$ V, V_{DS}=20 V.

while it maintains low calculation complexity and a good convergence behavior at the other hand. An extension accounting for three valleys is possible, was however ruled out due to the downgraded convergence.

3. Simulated devices

The epitaxial structures used in this work were grown by metal-organic chemical vapor deposition (MOCVD) on 3-in. semi-insulating SiC substrates. The layers consist of a highly-resistive c-plane GaN buffer, followed by a 22 nm thick $Al_{0.22}Ga_{0.78}N$ barrier and finally a 3 nm thin GaN cap layer (Fig. 6). Room temperature Hall measurements on the 2DEG formed at the buffer to barrier interface resulted in a sheet carrier concentration of 8×10^{12} cm^{-2} and a mobility of 1600 cm^2/Vs. After epitaxial growth, ohmic contacts were formed, showing a low contact resistance of 0.2 Ω mm. The nitride-assisted T-gate was used with two different gate lengths of 0.5 μm and 0.25 μm, and was defined by e-beam lithography. The gate width $W_g = 2 \times 50$ μm is taken as 1×100 μm in the simulation.

4. Simulation results

The $l_g = 0.25$ μm structure serves as a calibration device. Based on the transfer characteristics we determine the already mentioned values for the interface charges. Using the same set of models and model parameters the $l_g = 0.5$ μm benchmark device is simulated. The ambient temperatures at which the devices were measured and are simulated are 300 K, 365 K, and 425 K. For the gate-variation study, two more devices with $l_g = 0.1$ μm and $l_g = 0.15$ μm are simulated. Also a fourth ambient temperature of 485 K is explored.

4.1. DC results

Using the interface charges from Section 2.2 a very good agreement between measurement data and simulation results for the transfer characteristics of the calibration device ($l_g = 0.25$ μm) is achieved (Fig. 7). Our setup allows for a proper modeling of the drain current also at elevated temperatures. As an example, Fig. 8 shows the output characteristics at 425 K. Two curves are shown for $V_{GS} = 2$ V: without self-heating, which greatly overestimates the current; with self-heating, which delivers a significantly better match, but requires a higher computational effort.

While others [60] have observed a significant threshold voltage (V_{th}) shift, in our measurements such is almost non-existent. As V_{th} depends on the carrier density, carrier trap density and the Schottky barrier height [61] we can assume that trapping effects in the devices are also temperature-independent in this range (the carrier density change is also negligible).

Fig. 9 shows the lattice temperature in the device ($V_{DS} = 20$ V, $V_{GS} = 2$ V bias). The area where the lattice is heated from high-energy electrons is the high-electric field region under the drain side of the gate and the gate-extension.

The same simulations are performed for the benchmark device ($l_g = 0.5$ μm) next. Retaining the same interface charge values, a good prediction of the threshold voltage is obtained (Fig. 10). Raising the ambient temperature, once again yields a good agreement between simulation results and experimental data, also for the output characteristics (shown at 425 K in Fig. 11).

4.2. RF results

The RF device performance is studied by small-signal AC analysis [62]. Fig. 12 shows the current gain $|h_{21}|$ for the 0.25 μm device for the three temperatures. The gain decreases at higher

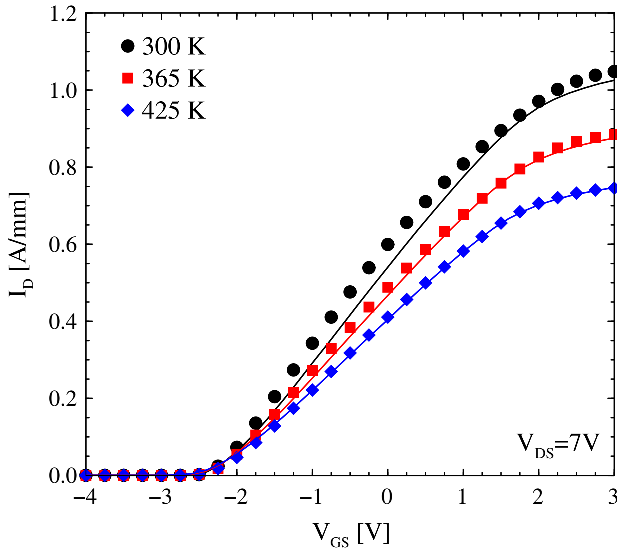

Fig. 10. Predicted transfer characteristics (lines) compared to measured data (symbols) for $l_g = 0.5$ μm HEMT.

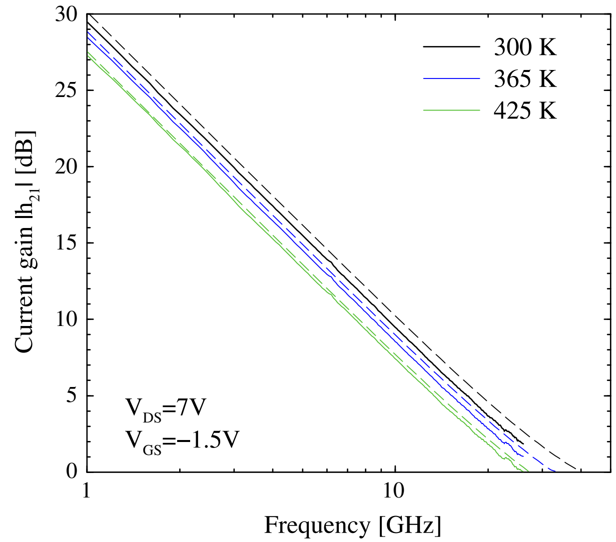

Fig. 12. Current gain $|h_{21}|$ for $l_g = 0.25$ μm HEMT, experimental data (solid lines) versus simulation (dashed lines).

temperatures and the simulation agrees well with the measurements. The calculated cut-off frequency f_T is compared to the measured in Fig. 13. In order to account for the parasitics introduced by the measurement equipment the intrinsic parameters delivered by the simulation are transformed into extrinsic ones by using a standard two-port pad parasitic equivalent circuit. The values of the circuit elements are: $L_S = 1$ pH, $L_G = 44$ pH, $L_D = 46$ pH, $C_{PGS} = 36$ fF, $C_{PGD} = 6$ fF, and $C_{PDS} = 9$ fF. As mentioned in Section 3 the measured device has two gate fingers of 50 μm width each, which leads to a higher gate capacitance due to three dimensional parasitic effects, than a single device with $W_g = 100$ μm as simulated.

We have achieved a very good agreement between measured and simulated S-parameters at all temperatures both for the calibration device ($l_g = 0.25$ μm) and the benchmark device ($l_g = 0.5$ μm). As an example, Fig. 14 compares the simulated and measured intrinsic S-parameters in the range 100 MHz–26 GHz at $V_{DS} = 7$ V and $I_D = 260$ mA/mm for the $l_g = 0.25$ μm HEMT at 300 K. Fig. 15 compares predictive simulation results for the $l_g = 0.5$ μm device in the same frequency range, $V_{DS} = 7$ V, and $I_D = 130$ mA/mm at 425 K.

4.3. Gate length variation

Geometry of the transistors is pointed out to be an important factor for high-temperature operation. Consequently, several authors have studied the reduction of I_D with rising temperature for different gate lengths e.g. [8,57]. They agree, that for short channel devices ($l_g < 1$ μm) the carriers travel under the gate with saturation velocity. Therefore, the decrease of I_D is lower, as the decrease of the velocity in the saturation region is also lower. While we study only submicron devices, our results for $l_g = 1.0$–0.25 μm structures agree well (Fig. 16) with those presented by Tan et al. However for very small gates an even lower temperature depen-

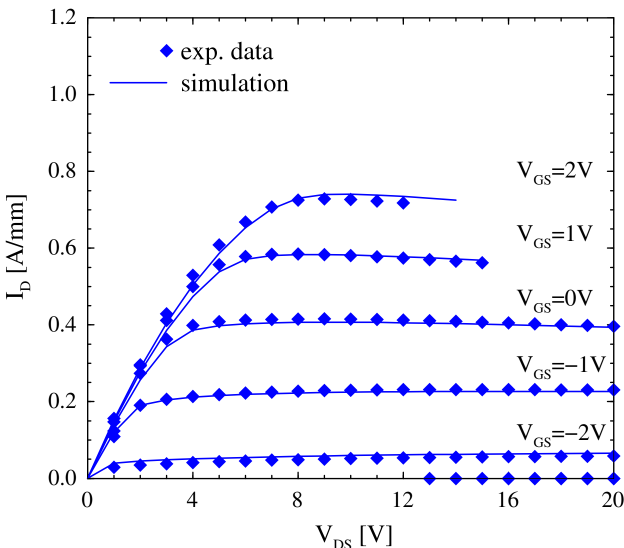

Fig. 11. Predicted output characteristics versus experimental data for $l_g = 0.5$ μm HEMT at 425 K.

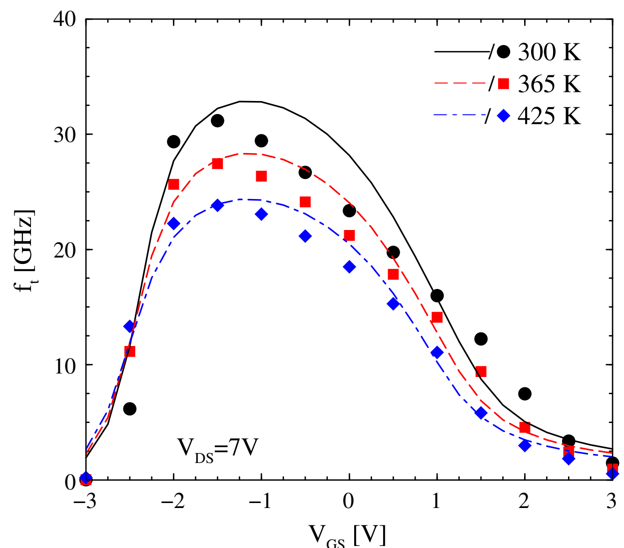

Fig. 13. Simulated cut-off frequency f_T (lines) compared to measurements (symbols) for $l_g = 0.25$ μm HEMT.

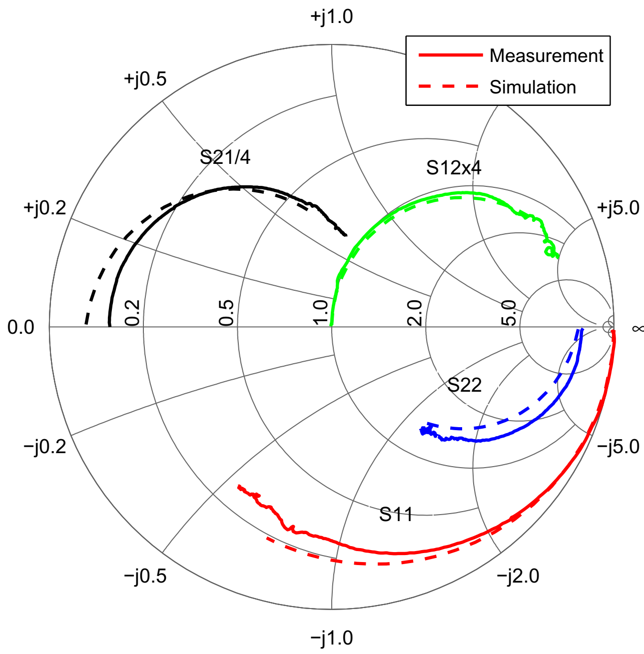

Fig. 14. S-parameters for the $l_g = 0.25$ µm device at 300 K.

dence is observed. This same effect is more pronounced for the normalized f_T, where the $l_g = 1.0–0.25$ µm devices deliver similar reduction of f_T with temperature, while the current gain cut-off frequencies of the sub-quartermicron devices decrease less (Fig. 17). We believe that for such gate lengths, not only l_g but also the gate-drain and gate-source distances and the exact geometry gain on importance, as for small gate lengths the parasitic contributions have to be scaled according to typical scaling rules in order to harvest the high-speed performance. In this case the relative contributions of the ohmic elements and thus their temperature dependencies are reduced.

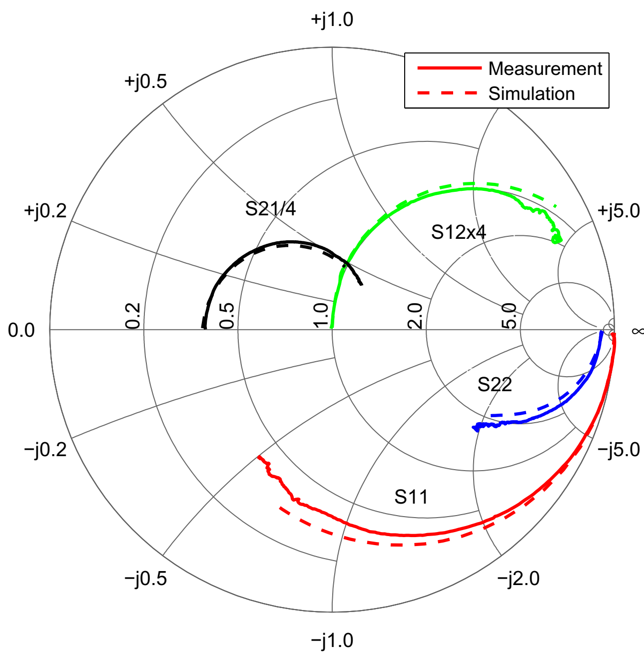

Fig. 15. S-parameters for the $l_g = 0.5$ µm device at 425 K.

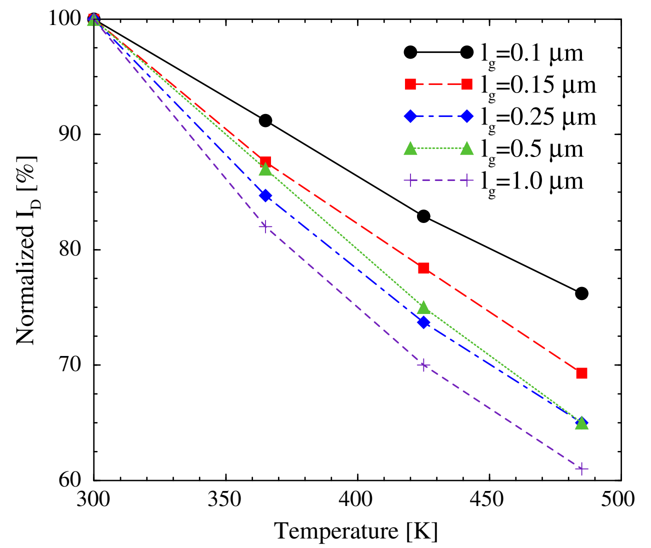

Fig. 16. Simulated maximum I_D ($V_{DS} = 7$ V) as a function of ambient temperature normalized to 300 K values.

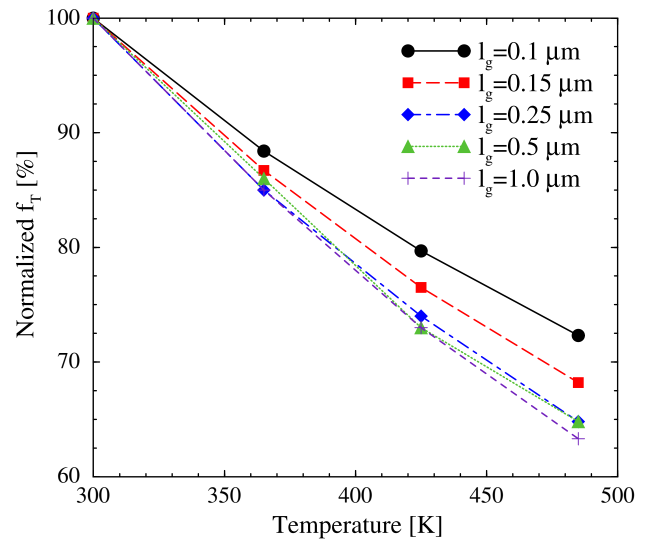

Fig. 17. Simulated maximum f_T ($V_{DS} = 7$ V) as a function of ambient temperature normalized to 300 K values.

5. Conclusion

A set of material and model parameters for hydrodynamic simulation of AlGaN/GaN HEMTs is presented. Relevant physical effects (such as self-heating) are accounted for. The set is validated against experimental data from a real device in a wide temperature range. Good predictive results for the DC and AC characteristics of another device are obtained. The calibrated simulation tool allows for the study, design and optimization of down-scaled structures for high-temperature operation.

Acknowledgment

The authors acknowledge support from Austrian Science Funds (FWF), Project START Y247-N13.

References

[1] Levinshtein M, Rumyantsev S, Shur M. Properties of advanced semiconductor materials. New York: Wiley; 2001.

[2] Palacios T, Chakraborty A, Rajan S, Poblenz C, Keller S, DenBaars S, et al. High-power AlGaN/GaN HEMTs for Ka-band applications. IEEE Electron Dev Lett 2005;26:781–3.
[3] Wu Y, Moore M, Saxler A, Wisleder T, Parikh P. 40-W/mm double fieldplated GaN HEMTs. In: Device research conference digest; 2006. p. 151–2.
[4] Quay R. Gallium nitride electronics. Berlin Heidelberg: Springer; 2008.
[5] Daumiller I, Kirchner C, Kamp M, Ebeling K, Kohn E. Evaluation of the temperature stability of AlGaN/GaN heterostructure FETs. IEEE Electron Dev Lett 1999;20:448–50.
[6] Arulkumaran S, Egawa T, Ishikawa H, Jimbo T. High-temperature effects of AlGaN/GaN high-electron-mobility transistors on sapphire and semi-insulating SiC substrates. Appl Phys Lett 2002;80(12):2186–8.
[7] Cuerdo R, Calle F, Brana A, Cordier Y, Azize M, Baron N, et al. High temperature behaviour of GaN HEMT devices on Si(111) and sapphire substrates. Phys Status Solidi A 2008;5(6):1971–3.
[8] Tan W, Uren M, Fry P, Houston P, Balmer R, Martin T. High temperature performance of AlGaN/GaN HEMTs on Si substrates. Solid-State Electron 2006;50(3):511–3.
[9] Akita M, Kishimoto S, Mizutani T. High-frequency measurements of AlGaN/GaN HEMTs at high temperatures. IEEE Electron Dev Lett 2001;22:376–7.
[10] Arulkumaran S, Ng G, Liu Z, Lee C. High temperature power performance of AlGaN/GaN high-electron-mobility transistors on high-resistivity silicon. Appl Phys Lett 2007;91(8):083516(3).
[11] Huque M, Eliza S, Rahman T, Huq H, Islam S. Temperature dependent analytical model for current–voltage characteristics of AlGaN/GaN power HEMT. Solid-State Electron 2009;53(3):341–8.
[12] Huq H, Islam S. AlGaN/GaN self-aligned MODFET with metal oxide gate for millimeter wave application. Microelectron J 2006;37(7):579–82.
[13] Chang Y, Zhang Y, Zhang Y, Tong K. A thermal model for static current characteristics of AlGaN/GaN high electron mobility transistors including self-heating effect. J Appl Phys 2006;99(4):044501(5).
[14] Chang Y, Tong K, Surya C. Numerical simulation of current/voltage characteristics of AlGaN/GaN HEMTs at high temperatures. Semicond Sci Technol 2005;20(2):188–92.
[15] Minimos-NT device and circuit simulator, user's guide, Release 2.0; 2002. <http://www.iue.tuwien.ac.at/mmnt>.
[16] Palankovski V, Quay R. Analysis and simulation of heterostructure devices. Wien/New York: Springer; 2004.
[17] Palankovski V, Vitanov S, Quay R. Field-plate optimization of AlGaN/GaN HEMTs. In: Tech. Dig. IEEE Comp. Semicond. IC Symp.; 2006. p. 107–10.
[18] Vitanov S, Palankovski V, Murad S, Roedle T, Quay R, Selberherr S. Predictive simulation of AlGaN/GaN HEMTs. In: IEEE compound semiconductor IC symposium; 2007. p. 131–4.
[19] Polyakov V, Schwierz F. Influence of electron mobility modeling on DC I–V characteristics of WZ-GaN MESFET. IEEE Trans Electron Dev 2001;48:512–6.
[20] Faraclas E, Anwar A. AlGaN/GaN HEMTs: experiment and simulation of DC characteristics. Solid-State Electron 2006;50(6):1051–6.
[21] Grasser T, Ting-Wei T, Kosina H, Selberherr S. A review of hydrodynamic and energy-transport models for semiconductor device simulation. Proc IEEE 2003;91(2):251–74.
[22] Vurgaftman I, Meyer J, Ram-Mohan L. Band parameters for III–V compound semiconductors and their alloys. J Appl Phys 2001;89(11):5815–75.
[23] Guo Q, Yoshida A. Temperature dependence of band gap change in InN and AlN. Jpn J Appl Phys 1994;33(5A):2453–6.
[24] Yoshida S, Misawa S, Gonda S. Properties of $Al_xGa_{1-x}N$ films prepared by reactive molecular beam epitaxy. J Appl Phys 1982;53(10):6844–8.
[25] Shan W, Ager J, Yu K, Walukiewicz W, Haller E, Martin M, et al. Dependence of the fundamental band gap of $Al_xGa_{1-x}N$ on alloy composition and pressure. J Appl Phys 1999;85(12):8505–7.
[26] Khan M, Skogman R, Schulze R, Gershenzon M. Properties and ion implantation of $Al_xGa_{1-x}N$ epitaxial single crystal films prepared by low pressure metalorganic chemical vapor deposition. Appl Phys Lett 1983;43(5):492–4.
[27] Ochalski T, Gil B, Lefebvre P, Grandjean N, Leroux M, Massies J, et al. Photoreflectance investigations of the bowing parameter in AlGaN alloys lattice-matched to GaN. Appl Phys Lett 1999;74(22):3353–5.
[28] Westmeyer A, Mahajan S, Bajaj K, Lin J, Jiang H, Koleske D, et al. Determination of energy-band offsets between GaN and AlN using excitonic luminescence transition in AlGaN alloys. J Appl Phys 2006;99(1):013705(4).
[29] Foxon C, Novikov S, Zhao L, Harrison I. Isoelectronic doping of AlGaN alloys with As and estimates of AlGaN/GaN band offsets. Appl Phys Lett 2003;83(6):1166–8.
[30] Schmitz A, Ping A, Khan M, Chen Q, Yang J, Adesida I. Schottky barrier properties of various metals on n-type GaN. Semicond Sci Technol 1996;11(10):1464–7.
[31] Zhou Y, Wang D, Ahyi C, Tin C, Williams J, Park M, et al. Temperature-dependent electrical characteristics of bulk GaN Schottky rectifier. J Appl Phys 2007;101(2):024506(4).
[32] Ambacher O, Foutz B, Smart J, Shealy J, Weimann N, Chu K, et al. Two-dimensional electron gases induced by spontaneous and piezoelectric polarization in undoped and doped AlGaN/GaN heterostructures. J Appl Phys 2000;87:334–44.
[33] Ambacher O, Majewski J, Miskys C, Link A, Hermann M, Eickhoff M, et al. Pyroelectric properties of Al(In)GaN/GaN hetero- and quantum-well structures. J Phys: Condens Matter 2002;14(13):3399–434.
[34] Yan W, Zhang R, Xiu X, Xie Z, Han P, Jiang R, et al. Temperature dependence of the pyroelectric coefficient and the spontaneous polarization of AlN. Appl Phys Lett 2007;90(21):212102(3).
[35] Sichel E, Pankove J. Thermal conductivity of GaN, 25–360 K. J Phys Chem Solids 1977;38(3):330. 330.
[36] Mion C, Muth J, Preble E, Hanser D. Thermal conductivity, dislocation density and GaN device design. Superlattices Microstruct 2006;40(4-6):338–42.
[37] Florescu D, Asnin V, Pollak F, Jones A, Ramer J, Schurman M, et al. Thermal conductivity of fully and partially coalesced lateral epitaxial overgrown GaN/sapphire (0001) by scanning thermal microscopy. Appl Phys Lett 2000;77(10):1464–6.
[38] Zou J, Kotchetkov D, Balandin A, Florescu D, Pollak F. Thermal conductivity of GaN films: effects of impurities and dislocations. J Appl Phys 2002;92(5):2534–9.
[39] Liu W, Balandin A. Thermal conduction in $Al_xGa_{1x}N$ alloys and thin films. J Appl Phys 2005;97(7):073710(6).
[40] Jezowski A, Danilchenko B, Bockowski M, Grzegory I, Krukowski S, Suski T, et al. Thermal conductivity of GaN crystals in 4.2–300 K range. Solid-State Commun 2003;128(2–3):69–73.
[41] Liu W, Balandin A. Temperature dependence of thermal conductivity of $Al_xGa_{1-x}N$ thin films measured by the differential 3 omega technique. Appl Phys Lett 2004;85(22):5230–2.
[42] Jacquot A, Lenoir B, Dauscher A, Verardi P, Craciun F, Stolzer M, et al. Optical and thermal characterization of AlN thin films deposited by pulsed laser deposition. Appl Surf Sci 2002;186(1-4):507–12.
[43] Slack G, Tanzilli R, Pohl R, Vandersande J. The intrinsic thermal conductivity of AlN. J Phys Chem Solids 1987;48(7):641–7.
[44] Slack G, Schowalter L, Morelli D, Freitas J. Some effects of oxygen impurities on AlN and GaN. J Cryst Growth 2002;246(3-4):287–98.
[45] Caughey D, Thomas R. Carrier mobilities in silicon empirically related to doping and field. Proc IEEE 1967;55(12):2192–3.
[46] Farahmand M, Garetto C, Bellotti E, Brennan K, Goano M, Ghillino E, et al. Monte Carlo simulation of electron transport in the III-nitride wurtzite phase materials system: binaries and ternaries. IEEE Trans Electron Dev 2001;48(3):535–42.
[47] Schwierz F. An electron mobility model for wurtzite GaN. Solid-State Electron 2005;49:889–95.
[48] Palankovski V, Marchlewski A, Ungersböck E, Selberherr S. Identification of transport parameters for gallium nitride based semiconductor devices. In: MATHMOD proceedings; 2006. p. 14–9.
[49] Joshi R. Temperature-dependent electron mobility in GaN: effects of space charge and interface roughness scattering. Appl Phys Lett 1994;64:223–5.
[50] Look D, Reynolds D, Hemsky J, Sizelove J, Jones R, Molnar R. Defect donor and acceptor in GaN. Phys Rev Lett 1997;79(12):2273–6.
[51] Molnar R, Götz W, Romano L, Johnson N. Growth of gallium nitride by hydride vapor-phase epitaxy. J Cryst Growth 1997;178(1-2):147–56.
[52] Mnatsakanov T, Levinshtein M, Pomortseva L, Yurkov S, Simin G, Khan M. Carrier mobility model for GaN. Solid-State Electron 2003;47(1):111–5.
[53] Dang X, Asbeck P, Yu E, Sullivan G, Chen M, McDermott B, et al. Measurement of drift mobility in AlGaN/GaN heterostructure field-effect transistor. Appl Phys Lett 1999;74(25):3890–2.
[54] Maeda N, Saitoh T, Tsubaki K, Nishida T, Kobayashi N. Two-dimensional electron gas transport properties in AlGaN/(In)GaN/AlGaN double-heterostructure field effect transistors. MRS Internet J Nitride Semicond Res 2000;S15(W4.7).
[55] Maeda N, Tsubaki K, Saitoh T, Kobayashi N. High-temperature electron transport properties in AlGaN/GaN heterostructures. Appl Phys Lett 2001;79(11):1634–6.
[56] Zanato D, Balkan N, Hill G, Schaff W. Energy and momentum relaxation of electrons in bulk and 2D GaN. Superlattices Microstruct 2004;36:455–63.
[57] Cuerdo R, Pedros J, Navarro A, Brana A, Pau J, Munoz E, et al. High temperature assessment of nitride-based devices. J Mater Sci: Mater Electron 2008;19(2):189–93.
[58] Albrecht J, Wang R, Ruden P, Farahmand M, Brennan K. Electron transport characteristics of GaN for high temperature device modeling. J Appl Phys 1998;83(9):4777–81.
[59] Donoval D, Florovic M, Gregusova D, Kovac J, Kordos P. High-temperature performance of AlGaN/GaN HFETs and MOSHFETs. Microelectron Reliab 2008;48(10):1669–72.
[60] Nuttinck S, Banerjee B, Venkataraman S, Laskar J, Harris M. High temperature performances of AlGaN/GaN power HFET. In: IEEE MTT-S international microwave symposium digest, vol. 1; 2003. p. 221–3.
[61] Arulkumaran S, Liu Z, Ng G, Cheong W, Zeng R, Bu J, et al. Temperature dependent microwave performance of AlGaN/GaN high-electron-mobility transistors on high-resistivity silicon substrate. Thin Solid Films 2007;515(10):4517–21.
[62] Wagner S. Small-signal device and circuit simulation, PhD thesis, Technische Universität Wien; 2005. <http://www.iue.tuwien.ac.at/phd/wagner>.